Determining Limits of Thermal NDT of Thick Graphite/Epoxy Composites

Vladimir VAVILOV, Institute of Introscopy, Tomsk, Russia

Abstract. The known approach to inspecting thin composites by using infrared thermography is extended onto thick graphite/epoxy samples where detecting defects at considerable depths requires careful optimization of a heating procedure and choosing a proper data processing algorithm.

1. Introduction

Graphite/epoxy composites are widely used in aero space and start to conquer other application areas, such as automotive industry, building, shipbuilding etc.
Modeling and data processing are indispensable research stages in developing most nondestructive testing (NDT) techniques. In thermal NDT, mathematical models allow better understanding the mechanisms which govern heat transfer in materials with subsurface defects, thus helping in evaluating detection limits. Analyzing thermal NDT models enables producing artificial images which can serve as references in the verification of data processing algorithms, including defect characterization.
In this paper, a closed-up approach to modeling, optimizing and data processing is discussed in the application to thermal NDT of graphite/epoxy composites.

2. Highlights of the approach

- Determining thermal properties of composites involved.
- Modeling defect situations.
- Optimizing an experimental procedure.
- Performing a test.
- Processing test results.
- Evaluating thermal NDT limits (by studying noise).
- Characterizing defects.

3. Determining composite thermal properties

It has been assumed that a graphite/epoxy composite is orthotropic and characterized by three components of thermal diffusivity: $\alpha_x, \alpha_y, \alpha_z$. The transverse z component has been determined by applying both a rear (R)-surface and front (F)-surface (Parker's) technique:

$$\alpha_z = 0.2656\, L^2 / \tau^*_{\min} \quad (F\text{-surface test}), \tag{1}$$

$$\alpha_z = 0.139\, L^2 / \tau_{1/2} \quad (R\text{-surface test}), \tag{2}$$

where L is the sample thickness, $\tau^*_{\min}$ is the specific heat transit time which specifies the minimum of the artificial function $\Theta = Fo^{1/3} T^F$, $Fo = \alpha_z \tau / L^2$ is the Fourier number, τ is the current time, $\tau_{1/2}$ is the half-rise time specified in $T^R(\tau)$, and $T^F(\tau)$, $T^R(\tau)$ are the *F*- and *R*-surface temperature evolutions.

The Parker's Eq. (2) is widely used in determining thermal diffusivity [1], while Eq. (1) is less known and its efficiency depends on how noisy is data (both multiplicative and additive noise might make difficult finding a $\tau^*_{\min}$ value) [2]. The graphite/epoxy α_z value determined by the Parker's method across the extended heated area was $3.28 \cdot 10^{-7}$ m^2/s (see Fig. 1 and Table 1).

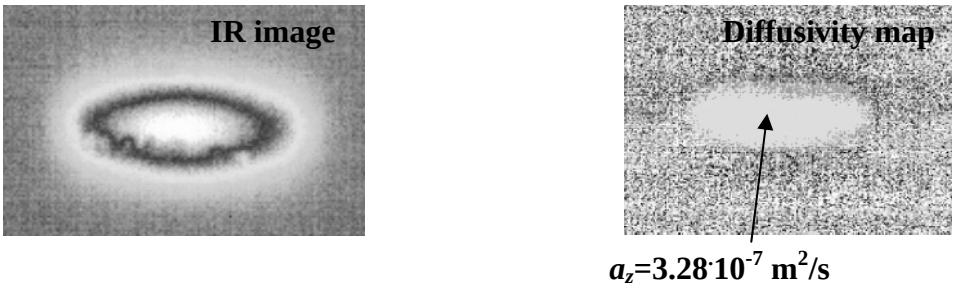

Fig. 1. Converting the *R*-surface IR image sequence into the diffusivity map (ThermoFit Pro program, Innovation Ltd, Russia)

The details of determining lateral components of graphite/epoxy thermal diffusivity have been reported elsewhere [3]. Both spot- and slit-mask techniques have been studied and the most reliable results have been obtained by using the latter one. Graphite/epoxy samples were heated by quartz lamps through a slit mask and the *R*-surface temperature was recorded by a Thermovision 570 IR imager with the acquisition frequency of 6 Hz. The algorithm applied is illustrated by Fig. 2. The spatial Fourier transformation is applied to a recorded IR image sequence (Fig. 2a). Due to the presence of the periodical temperature pattern, the Fourier spectrum clearly reveals the so-called carrier frequency (#5 in Fig. 2b if a mask contains 5 slits). The 'horizontal' (α_x) thermal diffusivity is determined by the slope of the function which represents the logarithmic ratio *LR* of two 'Fourier temperatures' obtained for non-zero and zero spatial frequencies [3]:

$$\alpha_{x,y}\,\tau = -\left[LR - c(\omega_{x,y}) \right] / \omega^2_{x,y}, \qquad (3)$$

where $LR = Ln[\overline{\overline{T}}(\omega_{x,y}, \tau) / \overline{\overline{T}}(0, \tau)]$ and $\omega_{x,y}$ is the respective spatial frequency. The experimental evolution of the *LR* function is shown in Fig. 2c and the determined lateral diffusivities are given in Table 1. The very convenient feature of Eq. (3) is that determining lateral diffusivity is not affected by sample optical semi-transparency and presence of heat exchange on *F*- and *R*-surface.

If a sample is heated with a square mask (or with a laser), both α_x and α_y components can be determined in a single experiment by analyzing both *x* and *y* spatial directions. In our case, the attempt of using a powerful Nd laser (pulse duration 1 ms) has proven to be inefficient due to dangerously high temperatures on *F*-surface and too low temperature on *R*-surface. Therefore, the heating was done with quartz lamps for 3 s and only *R*-surface data were used to calculate diffusivity. The experimental procedure was numerically optimized as described in [3].

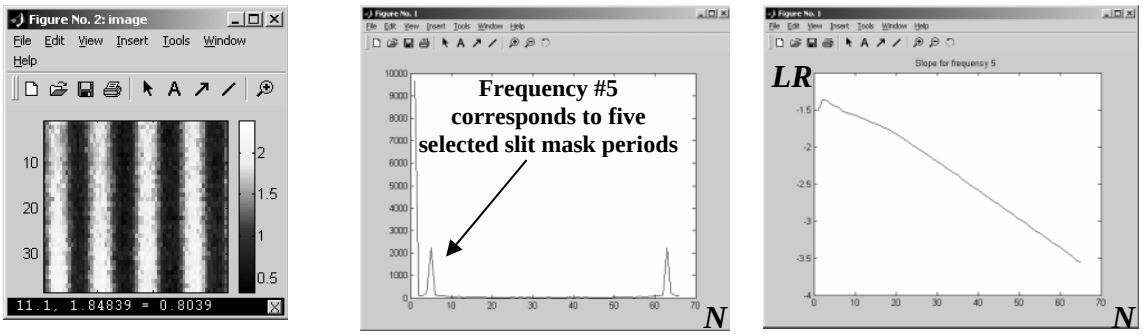

a) **b)** **c)**

Fig. 2. Evaluating thermal diffusivity by using a slit-mask method (graphite/epoxy sample, slit mask period 10 mm, heating time 3 seconds):

a – area of interest, Rear surface,

b - Fourier spectrum, α_x component (N-number of images in sequence),

c - $LR = Ln[\overline{\overline{T}}(\omega_{x,y},\tau)/\overline{\overline{T}}(0,\tau)]$ as a function of time

Table 1. Experimental graphite/epoxy thermal diffusivity values

α_x, 10^{-7} m^2/s	α_y, 10^{-7} m^2/s	α_z, 10^{-7} m^2/s
4.5-6.5	17.9-20.6	3.28 (±10%)

Thermal conductivity was measured with a TPMU-αλ-20 unit (Russia) to be λ_z=0.41 W/(m·K). Respectively, heat capacity was: $C\rho = \lambda_z / \alpha_z$ =1.25·10^6 J/(m^3·K).

4. Modelling defect situations

By introducing the determined values of thermal properties, over 100 defect situations were modeled using the ThermoCalc-6L program (Innovation Ltd., Russia). The program allows modeling a parallelepiped-like six-layer sample with up to nine parallelepiped-like defects (Fig. 3) uniformly or non-uniformly heated with a square pulse of a chosen duration (arbitrary heating functions and spatial heating masks are also possible). The following model parameters have been varied: sample thickness L =5, 10 and 15 mm, defect depth l =1,2,3,4,5,6,7,8 and 9 mm, defect thickness d =0.05, 0.1 and 0.2 mm, defect lateral dimensions 10x10, 20x20 and 50x50 mm, heating duration τ_h =0.01 and 10 s and heating power Q =10^6 and 10^4 W/m^2 respectively. Different carbon fibre lay-outs have been modelled to simulate technologies of producing thick graphite/epoxy composites.

Some examples of calculated data are presented in Table 2: $\Delta T_m^{F,R}$ - maximum differential signals on *F*, *R*-surface ($\Delta T = T_d - T_{nd}$, T_d, T_{nd} -defect and non-defect temperatures), $C_m^{F,R}$ - maximum dimensionless running contrasts ($C = \Delta T / T_{nd}$) with the corresponding optimum observation times τ_m. The data in Table 2 reveals 'classical' relationships between all involved parameters thus allowing: 1) optimizing a test procedure by heating power and duration, 2) evaluating thermal NDT limits, and 3) developing an inversion algorithm for characterizing defect depth, thickness and lateral dimensions.

5. Experimental set-up and test optimization

Both *F*- and *R*-surface test configurations have been implemented to test some graphite/epoxy samples with embedded Teflon inserts.

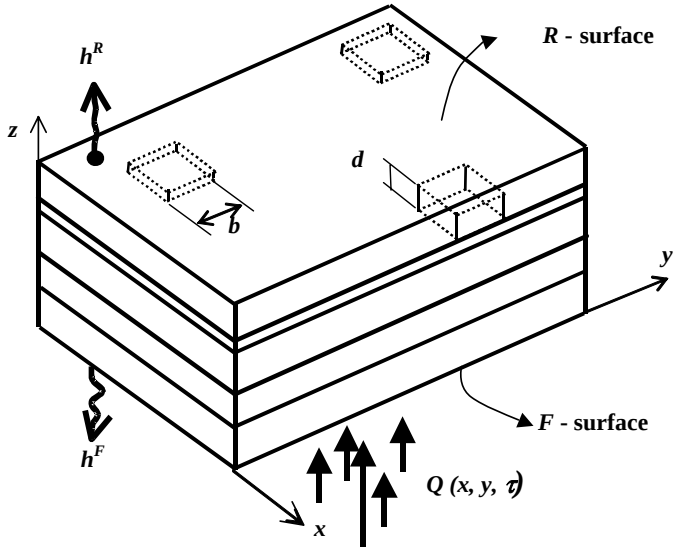

Fig. 3. 3D modeling of defects in graphite/epoxy composite

Table 2. Modeling thermal NDT of a 5 mm-thick graphite/epoxy composite

l, mm	d, mm	h, mm	ΔT_m^F, °C	$\tau_m^F(\Delta T)$, s	ΔT_m^R, °C	$\tau_m^R(\Delta T)$, s	C_m^F	$\tau_m^F(C)$, s	C_m^R	$\tau_m^R(C)$, s
Flash heating (τ_h =0.01 s, Q=10^6 W/m^2)										
1.0	0.05	10x10	0.343	2.42	-0.013	9.13	0.080	3.27	-0.189	2.24
		50x50	0.370	2.67	-0.025	10.41	0.094	4.10	-0.205	2.22
	0.1	10x10	0.601	2.61	-0.024	9.44	0.146	3.55	-0.267	2.16
		50x50	0.663	2.97	-0.047	10.88	0.178	4.70	-0.267	2.14
3.0	0.05	10x10	0.017	14.20	-0.025	11.33	0.010	16.60	-0.203	2.22
		50x50	0.038	18.15	-0.035	12.92	0.024	21.59	-0.205	2.22
	0.1	10x10	0.031	14.51	-0.045	11.61	0.018	17.00	-0.284	2.14
		50x50	0.072	18.85	-0.065	13.40	0.048	22.42	-0.287	2.14
Square-pulse heating (τ_h =10 s, Q=10^4 W/m^2)										
1.0	0.05	10x10	2.00	10.70	-0.121	15.60	0.062	11.60	-0.182	2.30
		50x50	2.58	10.90	-0.243	16.70	0.084	12.20	-0.196	2.30
	0.1	10x10	3.68	10.80	-0.219	15.90	0.117	11.80	-0.267	2.20
		50x50	4.92	11.10	-0.459	17.10	0.165	12.60	-0.286	2.20
3.0	0.05	10x10	0.169	20.20	-0.241	17.50	0.010	22.70	-0.193	2.30
		50x50	0.383	23.90	-0.350	18.90	0.025	27.40	-0.197	2.30
	0.1	10x10	0.307	20.50	-0.434	17.70	0.018	23.00	-0.281	2.20
		50x50	0.733	24.60	-0.662	19.30	0.049	28.20	-0.286	2.20

Samples were heated with the heater which consisted of six tubular quartz lamps of 5 kW power each that allowed heating a 0.4x0.4 m area with power density of about 15 kW/m^2. A typical image sequence included up to 300 images captured with a Thermovision 570 IR imager at 0.16 s acquisition interval.

An optimized test should provide a maximum signal to noise ratio $SNR = \Delta T(\tau) / \sqrt{\bar{\sigma}_n^2}$, where $\sqrt{\bar{\sigma}_n^2} = \sigma_n$ is the standard deviation of temperature in a non-defect area. It has been shown theoretically that such condition is reached if heating is performed with a heat pulse which is of the Dirac-nature in both time and space. However, Dirac-like heating is limited by possible destruction of a sample because of a higher

temperature at the end of pulse. To provide 'milder' heating, a square-pulse test procedure is often used. By a proper combination of pulse duration and power, a compromise between needed *SNR* values and sample temperature can be achieved. Modelling results, such as given in Table 2, are often used to optimize a test procedure. Calculations are facilitated by the fact that excess sample temperatures and differential temperature signals are linearly proportional to heating power, i.e. $T, \Delta T \square Q$, while the contrast C is independent on Q.

6. Experimental results and model verification

Some illustrations of experimental results and data processing are presented in Fig. 4 for a 15 mm-thick graphite/epoxy sample with Teflon inserts. Obviously, because of the large sample thickness, the *F*-surface test (Fig. 4 except 4c) has proven to provide better defect 'visibility' than the *R*-surface test (Fig. 4c). The Fourier transformation applied to the time evolution of pixel-based temperature functions $T(x, y, \tau)$ has been chosen as a primary processing technique intended for making decision on whether further processing has to be applied to experimental results.

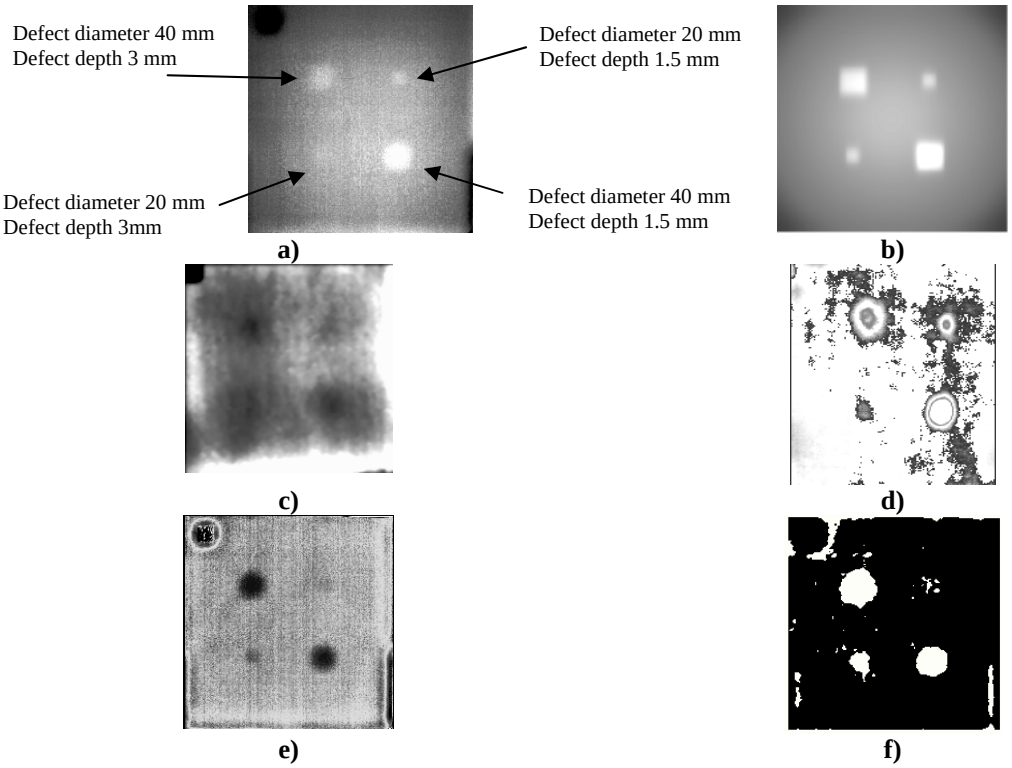

Fig. 4. Thermal NDT of a 15-mm thick graphite/epoxy sample (10 s heating):

a-raw image at the optimum observation time (*F*-surface),
b-same as a), simulation result (ThermoCalc-6L program),
c- raw image at he optimum observation time (*R*-surface),
d-same as a), after normalization,
e-phasegram,
f-binary map by e)

By computer modelling, it was immediately revealed that relatively big temperature signals which appeared over defects cannot be explained by the presence of Teflon inserts which should be in ideal thermal contact with a host composite. By multiple trial, it has been found that theoretical values match reasonably those experimental if to assume that

Teflon inserts are surrounded by air gaps with thickness from 0.06 to 0.1 mm (Fig. 5). The IR images calculated by such model resembled experimental IR thermograms very much (Fig. 4). It is worth mentioning that a similar model was proposed in the earlier paper where also the possibility of a slight modification of composite thermal properties over Teflon inserts was assumed [4].

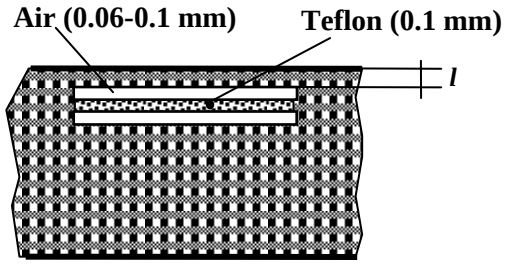

Fig. 5. The model of defects in a graphite/epoxy composite (Teflon inserts surrounded by air gaps)

The comparison between experimental and calculated data is given in Table 3. A relatively good match between these values favours the hypothesis of air-filled gaps between Teflon inserts and a host material.

Table 3. Comparing experimental and modelling data for a 15 mm-thick graphite/epoxy sample (Teflon inserts are surrounded by air gaps according to Fig. 6)

Defect	ΔT_m, **°C**	$\tau_m(\Delta T_m)$, **s**	$C_m = [\Delta T(\tau)/T(\tau)]_m$	$\tau_m(\Delta T_m)$, **s**
#1				
Experiment	4.2	13.2	0.14	16.4
Theory	*4.54*	*13.4*	*0.15*	*16.4*
#2				
Experiment	2.03	13.0	0.060	15.4
Theory	*2.57*	*12.8*	*0.081*	*14.8*
#3				
Experiment	1.08	21.6	0.070	44.6
Theory	*1.29*	*25.2*	*0.074*	*32*
#4				
Experiment	0.54	24.4	0.03	41.8
Theory	*0.89*	*23.2*	*0.046*	*27.6*

7. Noise and defect detection limits in thermal NDT

Studying noise is crucial in determining defect detection limits. As mentioned above, defects should produce a signal-to-noise ratio higher than unity ($S \geq 1$). Often the noise is classified for additive (IR detector noise and reflected ambient radiation) and multiplicative (structural noise). Then, the above-mentioned detection condition can be separated for the following ones: 1) a differential temperature signal ΔT must be higher than the temperature resolution ΔT_{res} of a used IR thermographic system, i.e. $\Delta T \geq \Delta T_{res}$ (the condition imposed by IR detector additive noise in the absence of reflected radiation), and 2) a running contrast C must be higher than a noise running contrast C_{noise}, i.e. $C = \Delta T / T_{nd} \geq C_{noise}$ (the condition imposed by multiplicative noise).

The second detection condition requires that a sample temperature must be under the temperature of *material destruction* T_{destr}, i.e. $T < T_{destr}$. Since a sample excess

temperature is linearly proportional to the absorbed energy W, this condition limits either heating power Q or heating duration τ_h (note that $W = Q\tau_h$).

Finally, IR thermographic systems can be characterized by their time resolution, i.e. by the image acquisition rate *f* which must be high enough to ensure a reasonable number of images stored before an optimum observation time τ_m is reached. This condition can be roughly assumed as follows: $f \geq (5...10)/\tau_m$.

In many thermal NDT cases, detection limits are conditioned by sample structural noise. By other words, each material can be characterized by the noise contrast C_{noise}. This kind of noise mainly comes from variations in sample emissivity/absorptivity. The minimum C_{noise} value of about 1-2% appears in case of uniform non-metals and/or materials covered with 'black coatings', such as soot, graphite enamel, oil paints etc.

The 1% threshold has been applied to all calculated data (see example in Table 2) to produce Table 4 where detection limits are presented for two sample thicknesses and both flash and square-pulse test procedures.

Table 4. Theoretical limits in detecting air-filled defects in graphite/epoxy composite (detection limit is assumed to be 1% by running temperature contrast)

Minimum detectable defects *			
***L*=5 mm**		***L*=15 mm**	
***F*-surface**	***R*-surface**	***F*-surface**	***R*-surface**
Flash heating			
l=4 mm (*D* =10 mm, *d*=0.1 mm)	At any depth (*D* =10 mm, *d*=0.1 mm)	*l*=5 mm (*D* =10 mm, *d*=0.5 mm)	*l*> ~ 4 mm (*D* =10 mm, *d*=0.5 mm)
l=3 mm (*D* =5 mm, *d*=0.1 mm)	At any depth (*D* =5 mm, *d*=0.1 mm)	*l*< 2 mm (*D* =5 mm, *d*=0.5 mm)	*l*> ~ 10 mm (*D* =5 mm, *d*=0.5 mm)
l=3 mm (*D* =10 mm, *d*=0.05 mm)	At any depth (*D* =10 mm, *d*=0.05 mm)	*l*< 2 mm (*D* =10 mm, *d*=0.25 mm)	*l*> ~ 5 mm (*D* =10 mm, *d*=0.25 mm)
Square-pulse heating			
l=4 mm (*D* =10 mm, *d*=0.1 mm)	*l*=4 mm (*D* =10 mm, *d*=0.1 mm)	*l*=5 mm (*D* =10 mm, *d*=0.5 mm)	At any depth (*D* =10 mm, *d*=0.5 mm)
l=3 mm (*D* =5 mm, *d*=0.1 mm)	*l*=3 mm (*D* =5 mm, *d*=0.1 mm)	*l*< 5 mm (*D* =5 mm, *d*=0.5 mm)	*l*> 2 mm (*D* =5 mm, *d*=0.5 mm)
l=3 mm (*D* =10 mm, *d*=0.05 mm)	*l*=3 mm (*D* =10 mm, *d*=0.05 mm)	*l*< 2 mm (*D* =10 mm, *d*=0.25 mm)	At any depth (*D* =10 mm, *d*=0.25 mm)

* l - defect depth counted from *F*-surface, D - defect diameter, d - defect thickness

The following conclusions are implicated by the data in Table 4.

- In practical cases, the predictions in Table 4 should be modified by two other detection conditions which have been discussed above. For example, available heat energy might be not enough to create a detectable ΔT signal. Then, a reasonably high temperature contrast may not be supported by an adequate differential temperature signal. Such situation is more likely on *R*-surface in case of thicker samplers and shorter heat pulses. Furthermore, on *F*-surface, a heat pulse of a particular energy may overheat a sample thus making test destructive.
- Minimum detectable defects are characterized by a combination of depth, thickness and lateral size. Simply, such defects can be deep but laterally extended, or small but thick, etc.
- In thin composites (*L*~5 mm), a two-sided test allows detecting defects through whole sample thickness, but in thick composites (*L*~15 mm), even a two-sided test requires defects to be located closer to *R*-surface. In all cases, the efficiency of a one-sided (*F*) test strongly depends on defect depth.

8. Enhancing defect visibility

Particular components of noise corrupting thermal NDT results can be subdued by proper data treatment. For example, temperature resolution of an IR system that represents the ultimate detection limit in thermal NDT can be improved by averaging temperature read-outs (with a respective loss of acquisition speed). Uneven heating can be seriously reduced by normalization (compare images in Fig. 4a and 4d). Surface phenomena largely disappear in phasegrams (Fig. 4e). Certain discrimination between defects can be done by applying polynomial fitting to temperature evolutions in time. A possible gain in *SNR* values cannot be predicted in advance and requires a special study by statistically comparing identification results by different processing algorithms [5]. In addition to the above-mentioned techniques, principal component analysis and neuron networks start to be effectively applied in thermal NDT. Using advanced data processing algorithms might improve the detection limits presented in Table 4.

9. Defect characterization

A great deal of inversion algorithms have been proposed to evaluate defect lateral size, depth l and thickness. A deeper analysis of these techniques is done in [2].
Defect lateral dimensions can be determined by: 1) simply viewing defect surface footprints that typically ensures accuracy of about 10-30%, 2) measuring the spatial extension of a ΔT signal at the half of maximum amplitude (FWHM - Full Width Half Maximum technique), 3) differentiating ΔT signal in space.

For determining l and d, some peculiarities in time evolution of ΔT or C are typically used (apparent effusivity, log-log data presentation etc.). In this study, we have used the following inversion formulas derived by fitting the data such as in Table 2 [2]:

$$l\ [m] = 0.7076\ [\alpha(\tau_m - \tau_h)]^{0.4564}(1-\lambda_d/\lambda)^{0.2849}(L/\lambda)^{0.05359} Fo_h^{0.05227} C^{-0.1511};$$
$$R_d[m^2 \cdot K \cdot W^{-1}] = 4.3682[\alpha(\tau_m - \tau_h)]^{0.3432}(1-\lambda_d/\lambda)^{1.2647}(L/\lambda)^{0.2862} Fo_h^{-0.05300} C^{0.4256}, \quad (4)$$

where λ_d is the thermal conductivity of a defect, $R_d = d/\lambda_d$ is the thermal resistance of a defect.

The accuracy of using Eq. (4) is typically better than 20% and 60% for l and R_d respectively.

10. Conclusions

- Implementing thermal NDT in the inspection of particular materials requires fulfilling some theoretical and experimental steps to optimize both a heating/recording protocol and data processing. These steps are: 1) determining thermal properties of materials, 2) modeling defect situations, 3) optimizing an experimental procedure, 4) performing a test, 5) processing test results, 6) evaluating thermal NDT limits (by analyzing noise), 7) characterizing defects.
- Defect situations are typically simulated numerically thus obtaining direct relationships between defect parameters, such as lateral dimensions, depth and thickness, and temperature signals (optimum observation times) caused by defects.

- Defect detection limits are determined by combinations of some conditions which require that: 1) a signal-to-noise ratio calculated by either differential temperature signals or dimensionless contrasts, or both, must exceed unity, 2) sample temperature during test must be under material destruction level, 3) acquisition frequency must be high enough to ensure reliable temperature recording and data processing at optimum observation times. Signal-to-noise ratio can be enhanced by applying some advanced processing algorithms, such as pulse phase thermography, principal component analysis, polynomial fitting, neural networks etc.
- In thin composites (L~5 mm), a two-sided test allows detecting defects through whole sample thickness, but in thick composites (L~15 mm), even a two-sided test requires defects to be located closer to R-surface. In all cases, the efficiency of a one-sided test strongly depends on defect depth and in most cases it does not exceed 4 mm.
- The fact of reliable detection of Teflon inserts in many experimental reference composite samples can be explained by the presence of air-filled gaps between inserts and a host material,
- Proposed inversion formulas allow determining depth and thermal resistance of defects in graphite/epoxy composites with the accuracy better than 20% and 60% respectively.

Conclusions

[1] W.J. Parker, R.J. Jenkins, C.P. Butler and G.L. Abbot, "Flash method of determining thermal diffusivity, heat capacity and thermal conductivity", *J. Appl. Physics*, Sept. 1961, Vol. 32, p.1679-1684.
[2] V.P. Vavilov, "Thermal NDT", *NDT series*, ed. Russian NDT Soc., Vol. 5, 2004, 384 p. (*in Russian*).
[3] V.P. Vavilov and D.D. Burleigh, "Determining thermal diffusivity components in thick anisotropic composites by using IR thermography", *SPIE Proc. "Thermosense-XXVIII"*, Vol. 6205, 2006, pp. 620519.
[4] V.P. Vavilov, D.D. Burleigh and A.G. Klimov, "Advanced modeling of thermal NDT problems: from buried landmines to defects in composites", *Proc. SPIE "Thermosense XXIV"*, Vol. 4710, 2002, pp. 507-521.
[5] V.P. Vavilov, "Evaluating the efficiency of data processing algorithms in transient thermal NDT", *Proc. SPIE "Thermosense XXVI"*, Vol. 5405, 2004, pp. 336-347.